

# Second Harmonic Generation in Gallium Phosphide Nano-Waveguides

Aravind P. Anthur,<sup>†,¶</sup> Zhang Haizhong,<sup>†,¶</sup> Yuriy Akimov,<sup>‡,¶</sup> Ong Junrong,<sup>‡,¶</sup>  
 Dmitry Kalashnikov,<sup>†</sup> Arseniy I. Kuznetsov,<sup>†</sup> and Leonid Krivitsky<sup>\*,†</sup>

<sup>†</sup>*Institute of Materials Research and Engineering, A\*STAR (Agency for Science, Technology and Research) Research Entities, 2 Fusionopolis Way, #08-03 Innovis, Singapore 138634.*

<sup>‡</sup>*Institute of High Performance Computing, A\*STAR (Agency for Science, Technology and Research) Research Entities, 1 Fusionopolis way #16-16 Connexis, Singapore 138632.*

<sup>¶</sup>*Equal contribution*

E-mail: leonid.krivitskiy@imre.a-star.edu.sg

## Abstract

We designed, fabricated and tested gallium phosphide nano-waveguides for efficient second harmonic generation (SHG). We demonstrate SHG in the visible range using low power continuous-wave pump in the optical communication O-band. In our structures, lower-order eigenmodes of the pump are phase matched to a higher order eigenmode of the second harmonic. We satisfy the phase-matching condition for the efficient SHG by varying the widths of the waveguides and tuning the wavelength of the pump. In addition, we simultaneously optimise the device geometry to achieve the maximum overlap integral between the pump and the second harmonic. Through these optimizations, we achieve a conversion efficiency of more than 0.3 %  $\text{W}^{-1}\text{cm}^{-2}$ . We also show the temperature tuning of the optimal phase matching wavelength. The

presented results contribute to the development of integrated photonic platforms with efficient nonlinear wave-mixing processes for classical and quantum applications.

One of the key challenges of integrated quantum photonics is that the most efficient detection, storage and manipulation of photons are done in the visible spectral range, whereas the most efficient transmission of photons occurs at the telecom wavelengths. Nonlinear processes can be exploited to bridge this gap.<sup>1,2</sup> The nonlinear material for the frequency conversion process should satisfy several requirements: transparency at both the telecom and the visible wavelengths, high nonlinearity and high refractive index to provide strong light confinement, which is essential for integrated photonic platforms. For these reasons, we have selected gallium phosphide (GaP) as the promising candidate for frequency-conversion. It has a high refractive index ( $\sim 3$  in the O-band), high second-order nonlinear parameter ( $d_{36}$  of  $\sim 50$  pm/V in the O-band), good thermal conductivity for temperature tuning and broad transparency range from 550 nm to 11  $\mu\text{m}$ .<sup>3-16</sup>

As the first step for developing an integrated GaP platform for frequency conversion, we demonstrate the second harmonic generation (SHG) in nano-waveguides. The SHG is a well-studied process, being first demonstrated in crystalline quartz back in 1961.<sup>17</sup> This experiment is often considered as the birth of nonlinear optics,<sup>17</sup> followed by a detailed theoretical description of the nonlinear optical processes.<sup>18</sup> SHG remains the most studied and widely applied second-order nonlinear process among others.<sup>19</sup> Over these years, SHG has been studied extensively and used in bulk crystals and waveguides for a broad variety of applications, including lasers, pulse measurements, quantum optics, spectroscopy and imaging to name a few.<sup>20-23</sup> Hence, more efficient platforms for SHG are always desirable for these applications. This motivates a strong interest in the community for studying SHG and other nonlinear frequency mixing processes in nano-structures made of a variety of materials. This approach promises miniaturization of optical devices and leads to the development of scalable on-chip solutions for applications in quantum and nonlinear optics.<sup>24,25</sup> A number of integrated platforms has been developed so far based on different nonlinear materials (lithium

niobate, gallium arsenide, aluminium nitride and gallium nitride), and their comparison is provided in the supplementary material.

In this work, we designed and fabricated GaP based nano-waveguides to achieve high efficiency for SHG via modal-phase matching and strong mode overlap. Our idea is illustrated in Fig. 1. Figure 1(a) shows the conversion of the red-shifted IR wavelength to the blue-shifted visible wavelength in a nonlinear medium. The conversion efficiency of this process depends on the phase matching and mode overlap integral between the pump and the SHG eigenmodes. As shown in Fig 1(b), when the phase mismatch between the pump and SHG modes is zero (perfect phase matching), the SHG power increases along the length of the waveguide. When the phase mismatch between the pump and the SHG eigenmode is high, then the SHG power oscillates along the length of the waveguide transferring power back to the pump. Another important criteria for good SHG conversion efficiency is the mode overlap between the SHG and the pump eigenmodes as illustrated in Fig. 1(c). The pump and the SHG eigenmodes with the lowest phase mismatch can have very low mode overlap. In order to achieve a good conversion efficiency for SHG, we optimize the device geometry to obtain an optimum dimension that provides the lowest phase mismatch and the highest mode overlap integral between the SHG and the pump eigenmodes, see Fig. 1(d). By adopting our design to the dedicated fabrication process, we increased the conversion efficiency from  $1.22 \times 10^{-4} \% \text{ W}^{-1}\text{cm}^{-2}$  in the first batch of devices (referred to as WG1 henceforth) to more than  $0.3 \% \text{ W}^{-1}\text{cm}^{-2}$  in the second one (referred to as WG2 henceforth). The theoretically estimated external and internal normalized conversion efficiency for the WG2 is  $3.85 \% \text{ W}^{-1}\text{cm}^{-2}$  and  $520 \% \text{ W}^{-1}\text{cm}^{-2}$  respectively. The coupling in and out of the device is realised by tapered couplers.

We consider two different waveguide designs. WG1 has the height of 215 nm, the top width varying from 280 nm to 420 nm and the side wall angle of 65 degrees. WG2 has the height of 330 nm, top width of 260 nm and the side wall angle of 85 degrees. Both WG1 and WG2 have a length of 1.5 mm excluding the tapered couplers. The tapered couplers have a

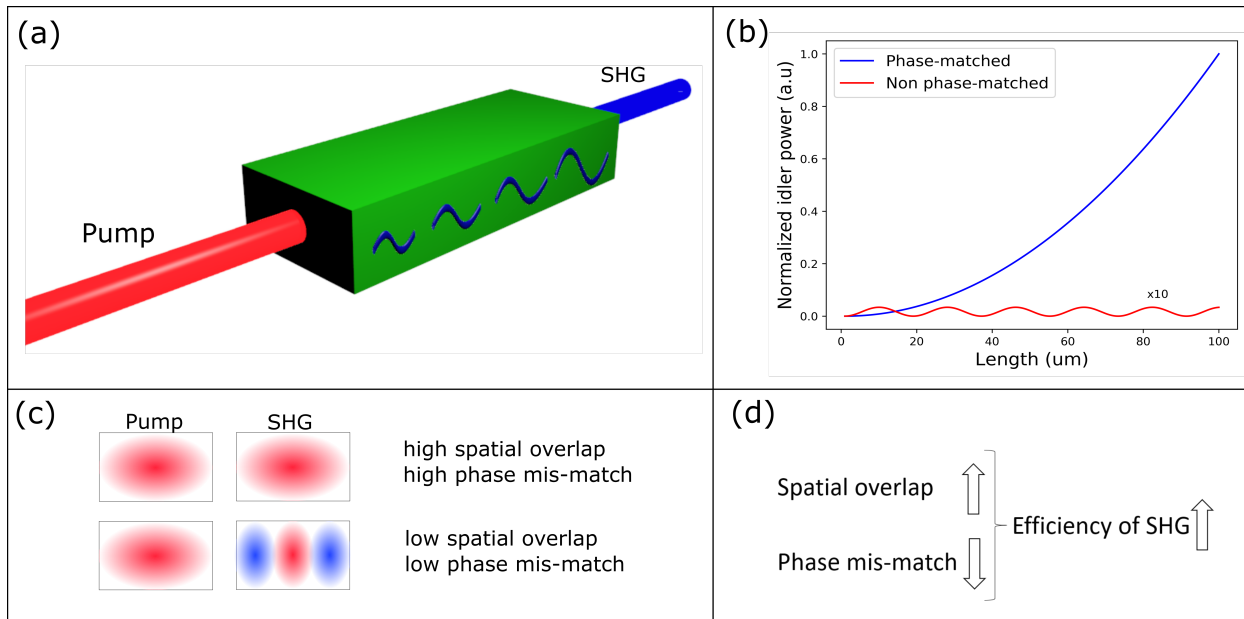


Figure 1: Principle of the generation of SHG in waveguides provided as an example where; (a) Red-shifted pump in the IR is converted to a blue-shifted SHG signal in the visible; (b) Normalized idler power as a function of the length for fully phase matched and non-phase matched propagation in nonlinear material; (c) Overlap between the fundamental and the SHG eigenmodes in the waveguide; (d) Dependence of the overlap integral and the phase mis-match on the overall SHG conversion efficiency.

length of 100  $\mu\text{m}$  on each facet. WG1 has a tapered coupler with the starting top width of 215 nm. WG2 has a tapered coupler with the starting top width of 100 nm.

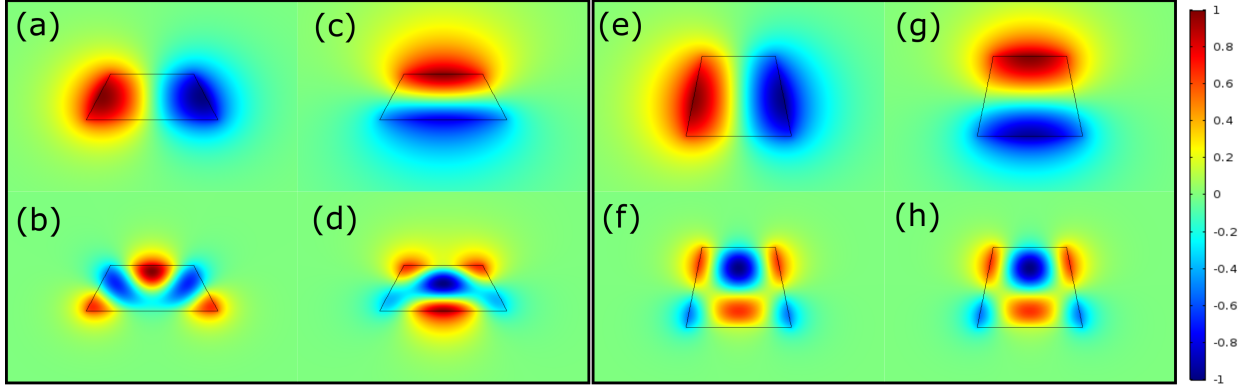


Figure 2: Dipolar eigenmodes of the first harmonic (FH) of the WG1 [(a), (c)] and WG2 [(e), (g)] waveguides; Phase matched higher-order eigenmode of the second harmonic in the WG1 [(b), (d)] and WG2 [(f), (h)] waveguide.

Following the coupled equations (as detailed in the supplementary material), the highest conversion efficiency of SHG is observed for the second-harmonic eigenmodes that are phase-matched and have high overlap integrals with dipolar eigenmodes of the first harmonic. We performed an optimization study by varying geometrical parameters of the waveguides and tuning the wavelength to identify those configurations that provide efficient SHG in the range of 630 nm to 680 nm for the dipolar first-harmonic eigenmodes. For the WG1, we found two second-harmonic eigenmodes that results in strong SHG. Figure 2(a, c) and Figure 2(b, d) show the simulated eigenmode profiles of  $E_z$  fields for the pump and the phase matched SHG modes, respectively. The efficient excitation of the second-harmonic eigenmode shown in Fig. 2(b) requires two first-harmonic eigenmodes plotted in Fig. 2(a, c), while the second-harmonic eigenmode shown in Fig. 2(d) requires only one first harmonic eigenmode plotted in Fig. 2(c). As for the WG2, we identified one second-harmonic eigenmode shown in Fig. 2(f) (Fig. 2(h) is the same as Fig. 2(f)) that enables strong SHG for any of the first-harmonic eigenmodes shown in Fig. 2(e, g). The similarity of Fig. 2(f) and Fig. 2(h) is due to the close effective indices of the dipolar modes shown in Fig. 2(e, g) that result in similar three-wave phase mismatch,  $\Delta\beta_{mnl}(\omega)$ .

We fabricated nanostructures on silicon dioxide ( $\text{SiO}_2$ ) on sapphire substrates. As shown in Fig. 3, the GaP device layer ( $\sim 400$  nm) is first grown on a gallium arsenide (GaAs) substrate by metal-organic chemical vapor deposition (MOCVD). Then this structure is directly bonded to the sapphire substrates after depositing  $\sim 2$   $\mu\text{m}$   $\text{SiO}_2$  layers on top of both surfaces. The GaAs substrate is then removed by wet etching. We start the fabrication of the GaP nano-waveguides with a standard wafer cleaning procedure (acetone, iso-propyl alcohol and deionized water in that sequence under sonication), followed by  $\text{O}_2$  and hexamethyl disilazane (HMDS) priming in order to increase the adhesion between GaP and subsequent spin-coated electron-beam lithography (EBL) resist of hydrogen silsesquioxane (HSQ). After spin-coating of HSQ layer with a thickness of  $\sim 540$  nm, EBL and development in 25% tetra-methyl ammonium hydroxide (TMAH) defines the nano-waveguide regions in HSQ. Inductively-coupled plasma reactive ion etching (ICP-RIE) with  $\text{N}_2$  and  $\text{Cl}_2$  is then used to transfer the HSQ patterns to GaP. Finally,  $\sim 3.2$   $\mu\text{m}$   $\text{SiO}_2$  cladding layer is deposited on top of the waveguides by ICP-CVD. Devices are diced using laser cutting for experimental testing. The cross-sectional scanning electron microscope (SEM) images of the WG1 and WG2 are given in Fig. 3(b) and Fig. 3(c), respectively.

Figure 4(a) shows the schematic of the experimental setup.<sup>26</sup> The pump light from a narrow linewidth continuous-wave tunable laser (Yenista, 1260 nm - 1360 nm, linewidth  $\sim 400$  kHz) is coupled into the waveguide using a tapered polarization-maintaining lensed fiber (OZ optics) designed for wavelengths around 1310 nm. We tune the pump wavelength from 1260 nm to 1360 nm in steps of 0.1 nm to offset the phase matching variations caused due to the uncertainty in the dimensions of the fabricated structures. An objective with a numerical aperture (NA) of 0.7 (Mitutoyo) is used to collect the higher-order second harmonic light output from the waveguide. The output from the objective is imaged using a charged coupled device (CCD) camera (uEye), which also gives the intensity readings. The CCD camera is preceded by a filter centered at 650 nm and having a bandwidth of 150 nm (Semrock). Another 10x objective and CCD camera is mounted above the structure to

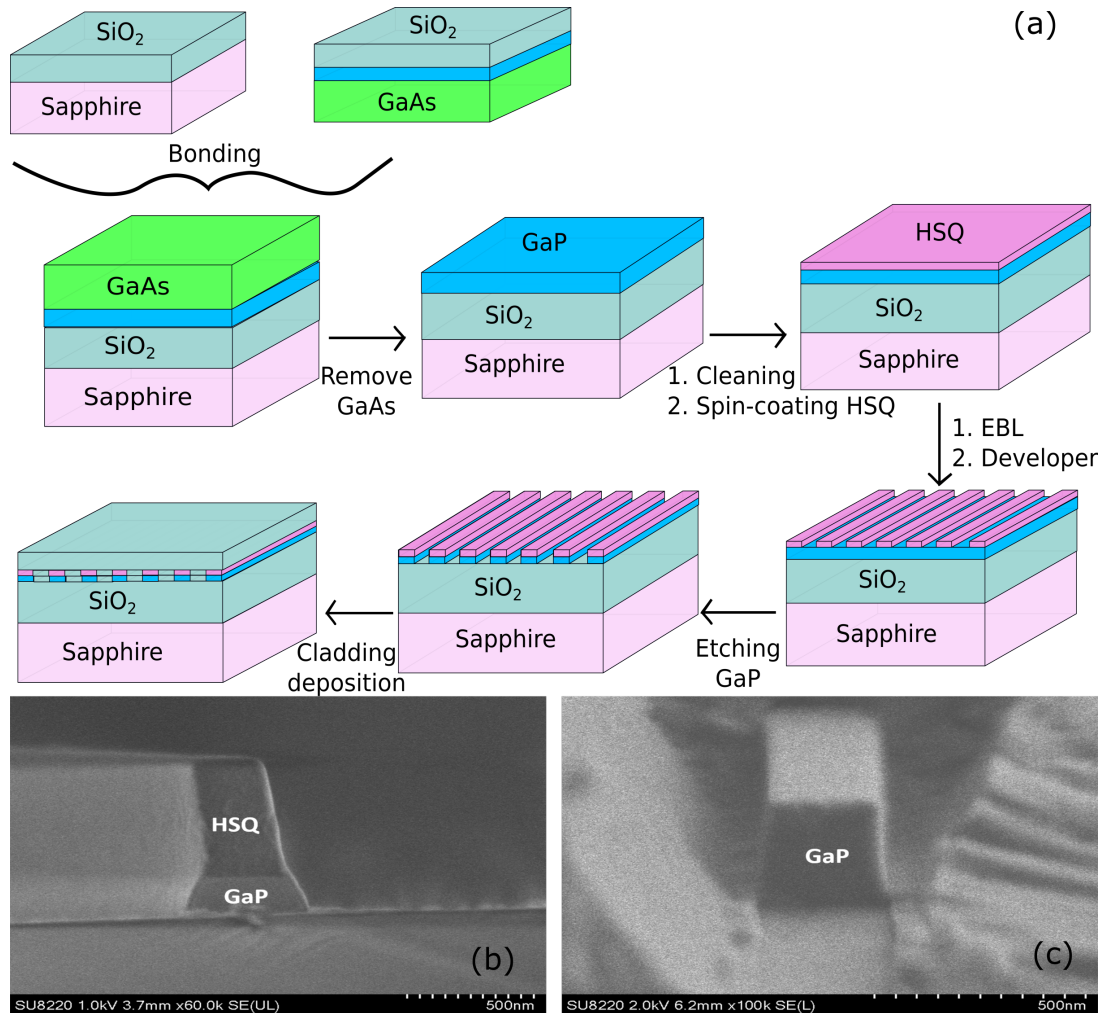


Figure 3: (a) Fabrication flow, refer to text for details; b) SEM image of waveguide with height of 215 nm and side wall angle of 65 degree (WG1); (c) SEM image of waveguides with height of 330 nm and side wall angle of 85 degree (WG2).

observe the interface with the fiber. A flip mirror is used to direct the SHG light into the spectrometer (Ocean Optics).

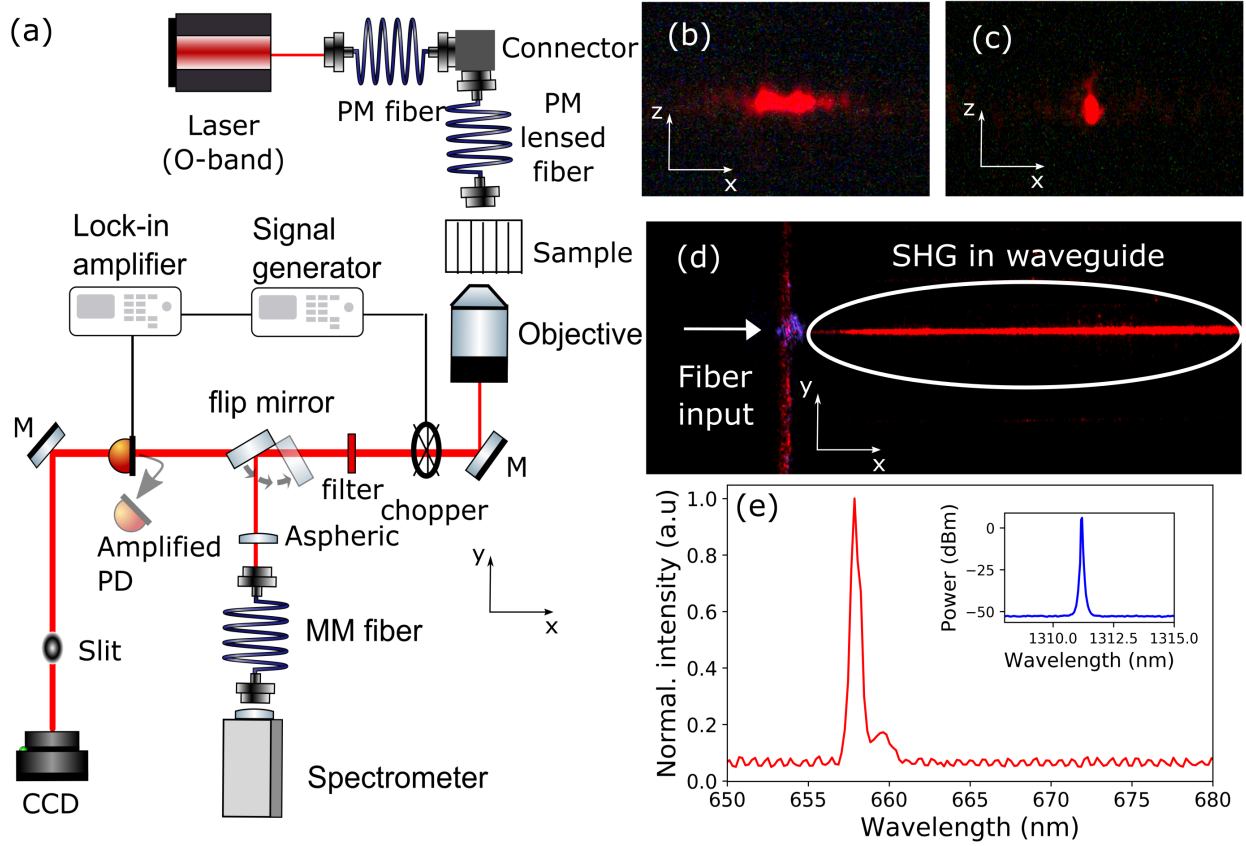


Figure 4: (a) Experimental setup showing tapered fiber input, chip mount, output objective to collect the second harmonic light, CCD camera used to analyze the second harmonic. CCD-camera, MM-multi mode, M-mirror, PM-polarization maintaining, PD photodetector; (b) SHG output from waveguide on the CCD camera for H polarized input pump in the WG1; (c) SHG output from the waveguide on the CCD camera for V polarized input pump in the WG1; (d) Top view of the waveguide when pump light is coupled into one of the waveguides in the WG2, with the waveguide marked using an ellipse where the SHG generation can be observed; (e) Spectrum of SHG with the pump spectra given in the inset.

The lock-in amplifier (Signal Recovery) is phase-locked to the chopper rotating at a frequency of 500 Hz, which is used for modulating the SHG signal, and to the amplified photo-detector (PD, Thorlabs) to detect the SHG signal. Since the chopper reduces the power by half, it is introduced at the output of the waveguide for SHG instead of the input pump because of the quadratic dependence between the pump power and the SHG power.

SHG is studied in the waveguide for horizontal (H) and vertical (V) pump polarizations.

The polarization of the pump is set by rotating the tapered lensed fiber and testing the output from the fiber through a polarizer without the waveguides in the path.

For temperature dependence studies, we attach a power resistor to the waveguide mount, which dissipates the heat and increases the temperature of the waveguide mount. The mount temperature is monitored and stabilized using a thermistor and temperature controller in a feedback loop with the precision better than 1 deg. C.

## Results

First we observe the mode structure of the SHG by using the CCD camera at the output of the chip. Figure 4(b) shows the SHG mode for the H polarized pump at 1330.7 nm in WG1 with the top width of 350 nm. Figure 4(c) shows the SHG mode for the V polarised pump at 1359.3 nm in WG1 with the top width of 310 nm. Figure 4(d) shows the image from the top CCD camera when pump light is coupled into the waveguide and there is SHG scattered by the waveguide. Figure 4(e) shows the spectrum of the SHG obtained from the spectrometer and the inset shows the optical spectrum of the pump light. The output SHG mode for WG2 for both H and V polarized input pump mode is similar to Fig. 4(c). It should be noted that the results presented in Fig. 4(b, c) are obtained after the tapered waveguide coupler, which affects the measured output mode profile of the SHG.

Next we study the variation of the SHG wavelengths as a function of the waveguide top width for H and V pump polarization in WG1. Figure 5 shows the dependence of the phase matched pump wavelength on the top width of the waveguide for H and V polarized input light. The blue dots (crosses) represent the experimentally obtained (simulated) phase-matched wavelengths for H polarized input as a function of waveguide top width. The red dots (crosses) show the experimentally obtained (simulated) phase-matched wavelengths for V polarized input pump as a function of waveguide top width.

In Fig. 5, we also show the experimental data and simulations of the phased matched

wavelengths obtained for WG2. We note that the WG2 have uniform fabricated dimensions. The green dot (crosses) represents the experimentally obtained (simulated) average phase matched wavelength for H polarized input. The magenta dot (crosses) represents the experimentally obtained (simulated) average phase matched wavelength for V polarized input.

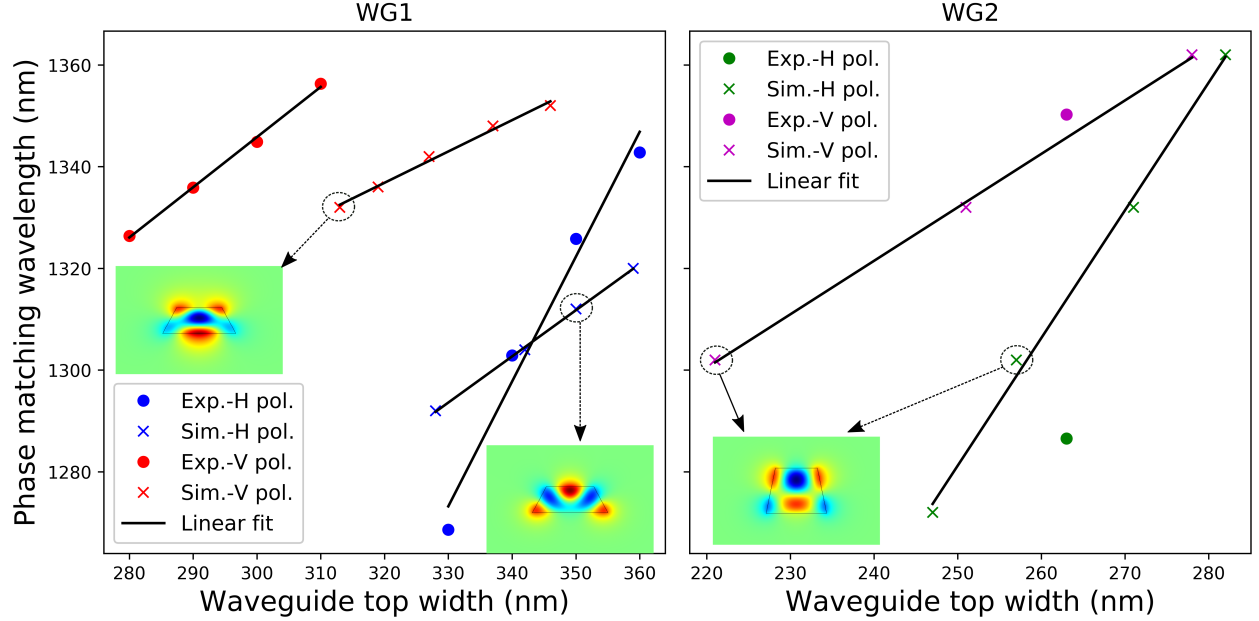


Figure 5: Experimental and simulated phase matched second harmonic wavelengths in waveguides for H and V polarized input pump light in WG1 and WG2. The simulations for WG1 are done for the side wall angle of 65 degrees and height of 215 nm. The simulations for WG2 are done for the side wall angle of 82 degrees and height of 260 nm. The SHG modes given in the inset and marked by arrows correspond to the results given in Fig. 2 (b, d and f (or h)).

Overall from Fig. 5, we observe that the experimental results for phase matching wavelengths for WG1 and WG2 for both H and V polarized inputs are closely following the simulations. The difference between the experimental and simulation results can be associated with the variations of dimension along the waveguide length and the side wall angle.

Next we performed the phase matching analysis in the WG2 structures. Figure 6 gives the phase matching bandwidth for one of the waveguide with the highest conversion efficiency. The top width of the waveguide is 215 nm, the height is 330 nm and the pump

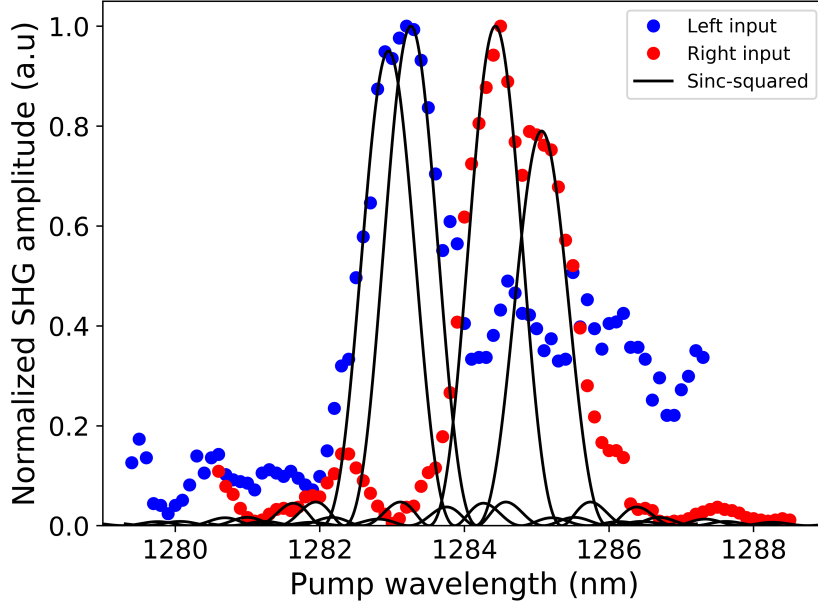


Figure 6: Normalized SHG counts as a function of pump wavelength and for H polarized input pump in one of the waveguides in WG2 for input pump from left (blue points) and right (red dots).

is H polarized. In Fig. 6, normalized SHG amplitude is plotted as a function of the pump wavelength. We tested the WG2 by coupling the pump either from the left side (blue points) or the right side (red points) of the waveguide. There are multiple sinc-squared functions plotted in Fig. 6 to show that the experimental data is affected by the non-uniformity and stitching errors in the waveguides.<sup>27</sup> From Fig. 6, we observe that, (1) there are multiple peaks for the SHG amplitude as the pump wavelength is varied and, (2) the phase-matching behaviour is different for pump input from the two different sides of the waveguide. These observations confirm that there are variations in the waveguide dimensions along the direction of propagation, which is consistent with the SEM data. The results in Fig. 6 also show that the effective interaction length for the average phase-matched wavelength is lower than 1.5 mm, which explains the lower experimental conversion efficiency compared to the theoretical predictions. We observe similar behaviour for the variation of SHG amplitude as a function of pump wavelength with two or more peaks for waveguides in WG1 and WG2.

Next we demonstrated the temperature tuning of the phase-matching wavelength. We

heat the the GaP nano-waveguides in sample WG2 from 22 °C to 100 °C. Figure 7 plots the variation of the phase-matching wavelength as a function of the set temperature of the waveguide mount. We observe over 13 nm tuning of the phase-matching wavelength. This corresponds to a slope of  $\sim 6$  (°C/nm), which is lower than the temperature slope of the commercially available periodically poled lithium niobate waveguide chip in this wavelength range.<sup>28</sup>

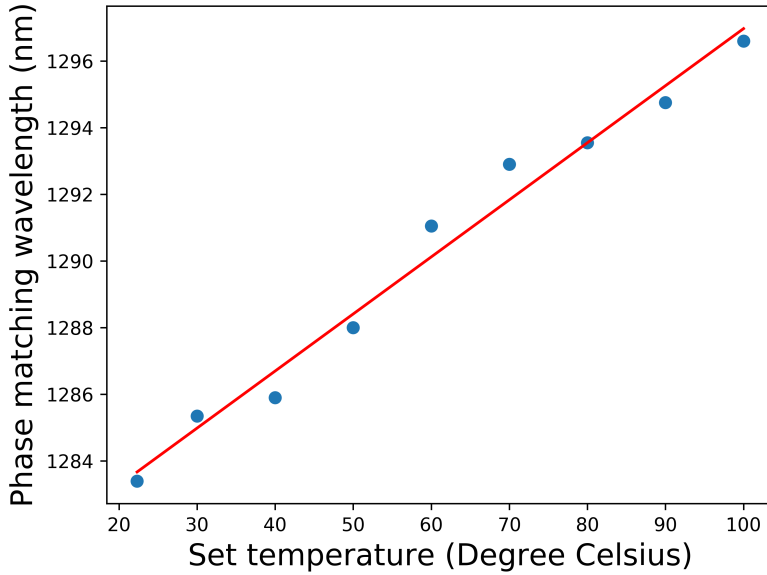


Figure 7: Experimental data for the temperature tuning of the phase matching wavelength (blue dots) for the nano-waveguide in WG2. Linear fit to the experimental data is given by red line.

The conversion efficiency of the SHG is measured using a low power continuous-wave laser tuned to the phase-matching wavelength of 1283.5 nm, see Fig. 6. For an optical pump power of 12.4 mW at the input of the waveguide, we measure a maximum SHG power of approximately 3.39 nW before the chopper (chopper reduces the SHG power by 50 %). This corresponds to a normalized SHG conversion efficiency of more than 0.3 %  $\text{W}^{-1}\text{cm}^{-2}$  for a waveguide length of 1.5 mm. It must be noted that this is an improvement by three orders of magnitude compared to the highest conversion efficiency obtained in WG1 waveguides of  $1.22\text{e-}4$  %  $\text{W}^{-1}\text{cm}^{-2}$ .

Even though the conversion efficiency for WG2 is the highest obtained value, we achieve

a conversion efficiency that is approximately within 10 % of this reported value in five out of eight fabricated waveguides. This demonstrates the stability of the design, fabrication and measurements. Moreover, we observed a direct correlation between the achieved conversion efficiency and the facet smoothness that in-turn depends on the laser dicing performance.

The total transmission for pump wavelengths in the waveguides in WG1 is approximately -10 dB. In WG2, we experimentally obtain the coupling loss/facet to be approximately 2.6 dB and propagation loss to be approximately 2.6 dB/mm, using nano-waveguides of varying lengths. The relatively high propagation loss in WG2 is currently under investigation and initial examination point towards the SiO<sub>2</sub> cladding roughness. The high propagation loss also contributes to the mismatch between the experimental and theoretical conversion efficiencies. Since the estimation of the coupling loss at the output for higher-order SHG mode is not possible, we provide the SHG conversion efficiency for WG2 using the pump power inside the waveguide and SHG power at the output of the waveguide. Thus, the normalized internal conversion of the WG2 is more than 0.3 % W<sup>-1</sup>cm<sup>-2</sup>. Supplementary material details the estimation of coupling and propagation loss in the WG2.

The dependence of the second harmonic power on the input pump power for WG2 is plotted in Fig. 8. The results are shown for H polarized input light and a phase-matched wavelength of 1283.3 nm. The blue dots (red line) represent the experimental data (fit). The second harmonic power varies as a function of the input pump power to the waveguide with a slope of approximately two in the log-scale, as expected from the theory. The inset in Fig. 8 shows the dependence of second harmonic counts as a function of input pump power for WG1. In this case, top width of the waveguide is 340 nm and the phase matching wavelength is 1303.1 nm.

For the WG1, we achieved the maximum external conversion efficiency of 1.22e-4 % W<sup>-1</sup>cm<sup>-2</sup>. By optimizing the design and fabrication, we achieved a maximum normalized conversion efficiency of more than 0.3 % W<sup>-1</sup>cm<sup>-2</sup> in the WG2. Simulations and analysis closely match the experimental results for both of the structures. The theoretically estimated

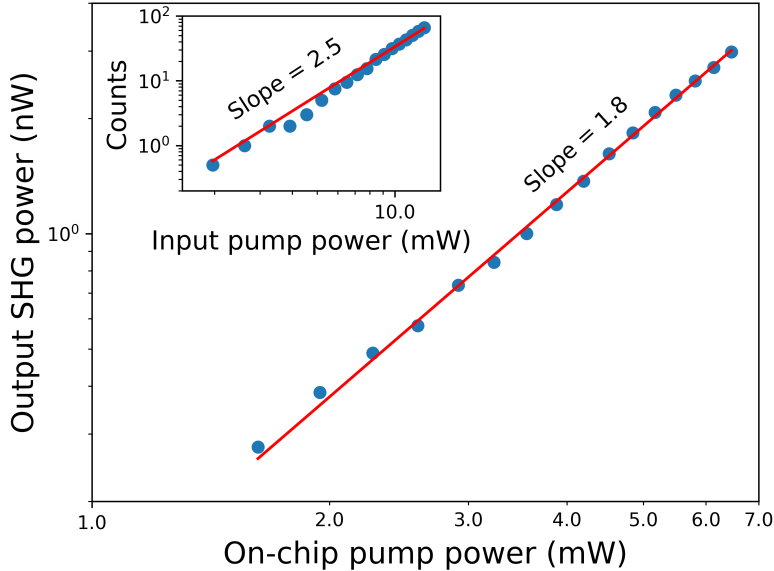


Figure 8: Dependence of output second harmonic power (blue dots) on the input pump power to the nano-waveguide in the WG2. (Inset) Dependence of output second harmonic counts (blue dots) on the input pump power into the nano-waveguide in the WG1. Quadratic fits to the experimental data is given by red lines. The R-squared of both of the fits are close to 1.

internal and external normalized conversion efficiency for the WG2 is 520 %  $W^{-1}cm^{-2}$  and 3.85 %  $W^{-1}cm^{-2}$ , respectively. There is an ongoing effort to improve the fabrication uniformity and optimize the device design to achieve higher conversion efficiencies. We also note the influence of the experimental uncertainty in the sizes of fabricated structures on the spectral properties of SHG signal. This suggests the possibility of using SHG as a tool for the analysis of performance of integrated nonlinear devices.

In conclusion, we designed gallium phosphide nano-waveguides for SHG using modal phase-matching and for achieving the highest mode overlap integral. The fabricated devices generated second harmonic for low power continuous-wave input pump at a phase-matched wavelength obtained by tuning the laser wavelengths from 1260 nm to 1360 nm. The variation of the experimentally obtained phase matched wavelength as a function of the waveguide top width and the phase matching bandwidth of the waveguides closely matches with the simulations. With the optimized design and fabrication, we achieved the normalized SHG conversion efficiency of more than 0.3 %  $W^{-1}cm^{-2}$  using continuous-wave low power

pump. The temperature tuning of the phase matching wavelength is demonstrated over 13 nm by heating the waveguide mounts from 22 °C to 100 °C. From our analysis of the literature,<sup>4,12,15,29–55</sup> the conversion efficiencies reported here are comparable in the III-V platform with non-resonant structures having cut off wavelength (band-gap) below 600 nm. This wavelength region is critical for quantum optics applications and the results demonstrated in this work will be useful for the development of nanophotonics nonlinear platforms for quantum optics.

## Acknowledgement

We thank Victor Leong for his help in designing and building experimental systems. We acknowledge the support of the Quantum Technology for Engineering (QTE) program of A\*STAR.

## Supporting Information Available

The following files are available free of charge. Supplementary material contains; (a) Detailed theoretical description; (b) The verification of the crystal axis of the sample used for fabricating the waveguides; (c) The results and estimation of the coupling and propagation loss in the waveguides in WG2; (d) Detailed summary of literature on second harmonic generation in nano-structures.

# Supplementary material: Second Harmonic Generation in Gallium Phosphide Nano-Waveguides

## Theory

In this work, we perform the optimization of waveguide parameters such that (1) a higher-order eigenmode of the second harmonic is phase matched to the dipolar eigenmodes of the pump, and (2) the mode overlap integral between the lower order eigenmode of the pump and the higher order eigenmode of the second harmonic signal is maximised.

The fields excited in the waveguide at the angular frequency  $\omega$  can be given as a superposition of eigenmodes,<sup>56</sup>

$$\mathbf{E}(\mathbf{r}, \omega) = \sum_m A_m(z, \omega) \tilde{\mathbf{E}}_m(x, y, \omega) e^{i\beta_m(\omega)z}, \quad (\text{S1})$$

where  $\mathbf{E}(\mathbf{r}, \omega)$  is the electric field,  $m$  is the eigenmode index,  $A_m(z, \omega)$  is the complex amplitude of the  $m^{\text{th}}$  eigenmode along the propagation direction ( $z$ ),  $\tilde{\mathbf{E}}_m(x, y, \omega)$  is the spatial distribution of the electric eigen field in the waveguide cross-section plane, and  $\beta_m(\omega)$  is the propagation constant of the  $m^{\text{th}}$  eigenmode. The eigen fields  $\tilde{\mathbf{E}}_m(x, y, \omega)$  are normalized by the condition,

$$-\frac{i}{2\mu_0\omega} \int \int \mathbf{e}_z \cdot \left( \tilde{\mathbf{E}}_m^*(x, y, \omega) \times \left[ \nabla \times \tilde{\mathbf{E}}_m(x, y, \omega) \right] \right) dx dy = 1 [W], \quad (\text{S2})$$

that corresponds to 1 W of total power transferred by the  $m^{\text{th}}$  eigenmode in the  $z$ -direction, where  $\mu_0$  is the vacuum permeability. Then, SHG is governed by the coupled equation,

$$\frac{dA_m(z, \omega)}{dz} = \frac{1}{2} \sum_{n,l} \kappa_{mnl}(2\omega, -\omega) A_n^*(z, \omega) A_l(z, 2\omega) e^{-i\Delta\beta_{mnl}(\omega)z}, \quad (\text{S3})$$

$$\frac{dA_m(z, 2\omega)}{dz} = - \sum_{n,l} \kappa_{mnl}^*(\omega, \omega) A_n(z, \omega) A_l(z, \omega) e^{i\Delta\beta_{nlm}(\omega)z}, \quad (\text{S4})$$

with the three eigenmode phase mismatch,  $\Delta\beta_{mnl}(\omega)$ , given by,

$$\Delta\beta_{mnl}(\omega) = \beta_m(\omega) + \beta_n(\omega) - \beta_l(2\omega), \quad (\text{S5})$$

and the overlap integrals,

$$\begin{aligned} \kappa_{mnl}(2\omega, -\omega) = i \frac{\omega\epsilon_0}{2} \sum_{i,j,k} \int \int \chi_{ijk}^{(2)}(x, y, \omega, 2\omega) \left[ \tilde{\mathbf{E}}_m^*(x, y, \omega) \cdot \mathbf{e}_i \right] \left[ \tilde{\mathbf{E}}_n^*(x, y, \omega) \cdot \mathbf{e}_j \right] \\ \times \left[ \tilde{\mathbf{E}}_l(x, y, 2\omega) \cdot \mathbf{e}_k \right] dx dy [W^{-1}], \end{aligned} \quad (\text{S6})$$

$$\begin{aligned} \kappa_{mnl}(\omega, \omega) = i \frac{\omega\epsilon_0}{2} \sum_{i,j,k} \int \int \chi_{ijk}^{(2)*}(x, y, \omega, \omega) \left[ \tilde{\mathbf{E}}_m^*(x, y, 2\omega) \cdot \mathbf{e}_i \right] \left[ \tilde{\mathbf{E}}_n^*(x, y, \omega) \cdot \mathbf{e}_j \right] \\ \times \left[ \tilde{\mathbf{E}}_l(x, y, \omega) \cdot \mathbf{e}_k \right] dx dy [W^{-1}]. \end{aligned} \quad (\text{S7})$$

The second-order susceptibility tensor,  $\chi_{ijk}^{(2)}(x, y, \omega, 2\omega)$ , that defines the overlap integrals strongly depends on the waveguide composition. For waveguides made of GaP and embedded in the second-order inactive materials such as silicon dioxide,  $\chi_{ijk}^{(2)}(x, y, \omega, 2\omega)$  strongly depends on its crystal orientation with respect to the waveguide. In the crystal axis basis  $(x', y', z')$ , it is given by the nonlinear tensor,  $d$ , under the Kleinman symmetry conditions,<sup>19</sup>

$$d = \begin{pmatrix} 0 & 0 & 0 & d_{36} & 0 & 0 \\ 0 & 0 & 0 & 0 & d_{36} & 0 \\ 0 & 0 & 0 & 0 & 0 & d_{36} \end{pmatrix}. \quad (\text{S8})$$

In our analysis, we assume  $d_{36} = 50 \text{ pm/V}$ .<sup>57</sup> As the crystal axis basis  $(x', y', z')$  is not necessarily the same as the waveguide axis basis  $(x, y, z)$ , it is important to do the rotational transformation between the two bases for calculation of the overlap integrals. In our case, the crystal axis orientation of GaP is confirmed to be tilted. This observation is made from the comparison of the experimental measurements with numerical simulations, details of which

are given in the next section.

## Measurement of crystal axis orientation

The crystal axis of the thin film gallium phosphide (GaP) sample that is used for fabricating the devices is rotated 15 degrees towards the  $[1\bar{1}1]$  as per the information provided by the vendor. This is verified by rotating the GaP thin film from 0 to 180 degrees around the normal to the thin film, measuring the second harmonic generation (SHG) from the thin film under the normal incidence of the pump and comparing the obtained experimental data with the simulations.

Figure S9 shows the schematic of the experimental setup.<sup>26</sup> The pump is a pulsed optical parametric oscillator (OPO) at 1310 nm, pumped by a Ti-Sapphire oscillator with the spectral width of 11 nm and repetition rate of approximately 78 MHz. Di-chroic beam splitter is used to spectrally filter the pump pulses from the OPO at 1310 nm. The light from the output of the di-chroic passes through a polarizer to increase the extinction of the polarized output from the OPO. The light then passes through a plano-convex lens and focusses at the thin film sample of GaP. The objective lens with an NA of 0.45 then collects the output from the thin-film. The light at the output of the thin film GaP sample contains both the pump and the SHG signal. A di-chroic beam splitter and filter are used to filter the SHG from the sample at the wavelength of approximately 655 nm. The filtered SHG signal is then collected and analyzed using a spectrometer.

The sample is rotated over 180 degrees around its normal and the amplitude of the SHG is analyzed as a function of the rotation angle of the sample. The angle of 0 degrees corresponds to the horizontally polarized input pump light. Figure S10 present the results. The experimental data (blue dots) is compared with the simulation results (red line) to verify that the crystal axis is rotated by 15 degrees towards the  $[1\bar{1}1]$  axis. This is critical to the design of the nano-waveguides.<sup>58,59</sup> There is a small angular shift of approximately 3 degrees



between the simulation and the experiment, that is compensated in Fig. S10, due to the rotation of the 0 degree definition in the experimental system.

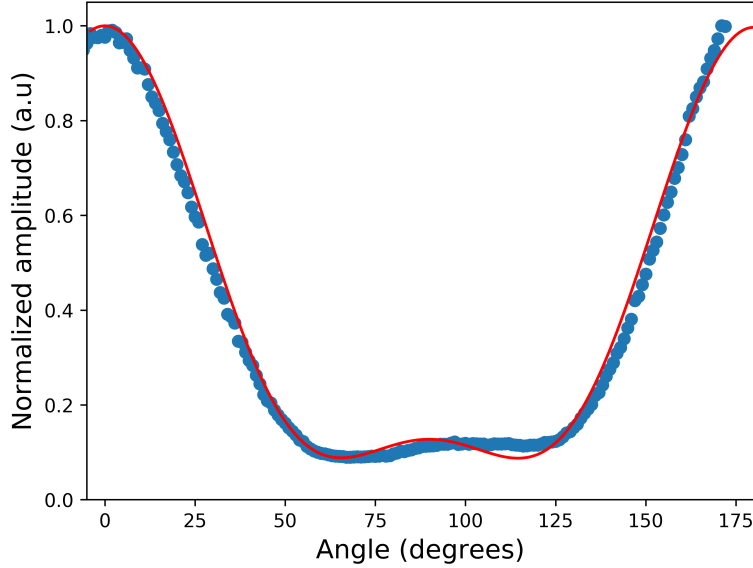


Figure S10: Experimental (blue dots) and simulated normalized SHG amplitude (red line) as a function of the rotation angle of the sample.

## Loss estimation of waveguides

The Figure S11 gives the transmission in dB as a function of waveguide length in WG2 batch of waveguides. The blue dots represent the experimental data. The green continuous line with stars represent the fitted data. The black discontinuous line shows the extended plot of the fit to show the y-intercept (total coupling loss). From the fit and using the following equation,

$$P_{out} = P_{in} \times T_{coupl}^2 \times e^{-\alpha l}, \quad (\text{S9})$$

we obtain the coupling and propagation loss of the fabricated structures in the WG2 batch. In the Eq. S9,  $P_{out}$  is the power measured with the waveguide in the beam-path,  $P_{in}$  is the power measured without the waveguide in the beam-path,  $T_{coupl}$  is the transmission through the coupler,  $\alpha$  is the attenuation constant, and  $l$  is the length of the waveguide.

The y-intercept in Fig. S11 is divided by two to obtain the coupling loss per facet and is approximately of 2.6 dB. The slope of the curve fit in Fig. S11 gives the propagation loss and is approximately of 2.6 dB/mm.

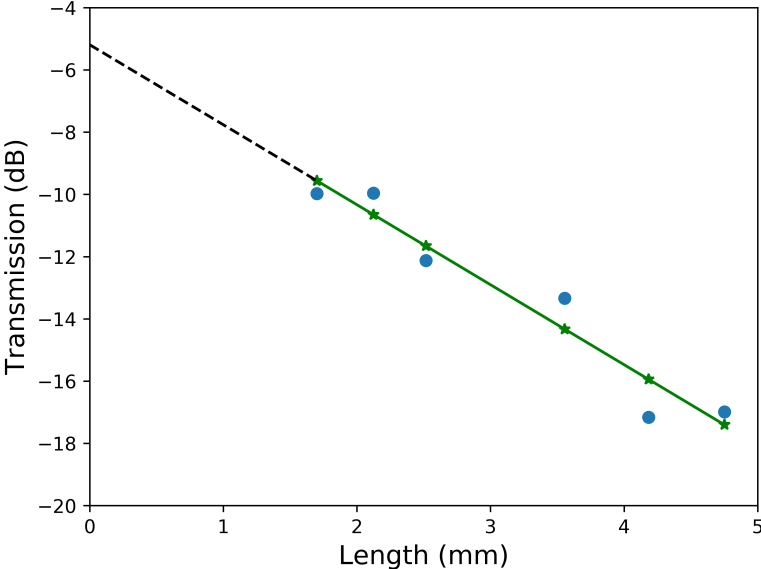


Figure S11: Experimentally obtained transmission (blue dots) through the waveguides in WG2 batch with different lengths and the curve fitting the results (green continues line with stars). The R-squared of the fit is of 0.93.

# Literature summary of second harmonic generation in nano-structures

Reference	Platform	Efficiency	Pump
35	Lithium niobate based resonators	1500 % $W^{-1}$	1547.1 nm (CW)
33	SiN waveguide on thin film lithium niobate	1160 % $W^{-1}cm^{-2}$	1574 nm (CW)
36	SiN waveguide on lithium niobate thin film	160 % $W^{-1}cm^{-2}$	1530 nm (CW)
37	Lithium niobate on insulator waveguides	26 % $W^{-1}cm^{-2}$ (Internal)	1550 nm (Pulsed)
41	Periodically poled lithium niobate	600 % $W^{-1}cm^{-2}$ (External)	851.7 nm (Pulsed)
44	Titanium in-diffused lithium niobate waveguide resonator	38 % $W^{-1}cm^{-2}$ (External)	1550 nm (CW)
46	Gradient metasurface based on Si on lithium niobate substrate	1660 % $W^{-1}cm^{-2}$ over metasurface length (Internal)	1640 nm (CW)
47	Lithium niobate nano-waveguides	41 % $W^{-1}cm^{-2}$ (Internal)	1574 nm (CW)
54	Periodically poled thin film lithium niobate	3.3% $W^{-1}$	1530 nm (CW)
55	Thin-film lithium niobate waveguide	48 % $W^{-1}cm^{-2}$ (External)	1385 nm (CW)

52	AlN waveguides and resonators	-24.7 dB- $W^{-1}cm^{-2}$ (Internal)	1550 nm (CW)
53	AlN double resonator	2500 % $W^{-1}$ (Internal)	1550 nm (CW)
30	AlN double resonator	17000 % $W^{-1}$ (Internal)	1590 nm (CW)
31	GaAs waveguide	13000 % $W^{-1}cm^{-2}$ (Internal)	2000 nm (CW)
34	AlGaAs waveguide	1202 % $W^{-1}cm^{-2}$ (Internal)	1560 nm (Pulsed)
42	GaN planar waveguide	0.15 % $W^{-1}cm^{-2}$	1260 nm (Pulsed)
45	GaAs waveguide	1.3 % (External)	2010 nm (Pulsed)
48	AlGaAs waveguide	$1.4 \times 10^4$ % $W^{-1}cm^{-2}$ (Internal)	1555 nm (Pulsed)
49	AlGaAs/Al <sub>2</sub> O <sub>3</sub> multilayer waveguide	0.12 % $W^{-1}$	1605 nm (Pulsed)
50	GaAs/Al <sub>2</sub> O <sub>3</sub> waveguide	1000 % $W^{-1}cm^{-2}$ (External)	2010 nm (Pulsed)
51	AlGaAs/Al <sub>x</sub> O <sub>y</sub> multi-layer waveguide	5 % $W^{-1}$ (Internal)	1570 nm (CW)
39,40	Multi-layered AlGaAs waveguide	13.8 % $W^{-1}cm^{-2}$ (Internal)	1582.6 nm (CW)

38	Periodically poled GaN	12.76 % $W^{-1}cm^{-2}$ (Internal)	1658.6 nm (Pulsed)
29	GaP photonic crystal cavity	430% $W^{-1}$ (Internal)	1550 nm (CW)
43	GaP micro disk	$3.8 \times 10^{-4}$ $mW^{-1}$ (External)	1545 nm (CW)
12	GaP micro-resonator	400 % $W^{-1}$ (Internal)	1550 nm (CW)
4	GaP photonic crystal waveguide	$5 \times 10^{-7}$ $W^{-1}$ (External)	1561.5 nm (CW)
15	InGaP nano-waveguide	0.2 % $W^{-1}cm^{-2}$ (External)	1572 nm (CW)
This work	GaP nano-waveguides	0.3 % $W^{-1}cm^{-2}$	1310 nm (CW)

## References

- (1) De Greve, K.; Yu, L.; McMahon, P. L.; Pelc, J. S.; Natarajan, C. M.; Kim, N. Y.; Abe, E.; Maier, S.; Schneider, C.; Kamp, M.; Höfling, S.; Hadfield, R. H.; Forchel, A.; Fejer, M. M.; Yamamoto, Y. Quantum-dot spin-photon entanglement via frequency downconversion to telecom wavelength. *Nature* **2012**, *491*, 421–425.
- (2) Zaske, S.; Lenhard, A.; Keßler, C. A.; Kettler, J.; Hepp, C.; Arend, C.; Albrecht, R.; Schulz, W. M.; Jetter, M.; Michler, P.; Becher, C. Visible-to-telecom quantum frequency conversion of light from a single quantum emitter. *Physical Review Letters* **2012**, *109*, 147404.

- (3) Van Der Ziel, J. P.; Mikulyak, R. M.; Cho, A. Y. Second harmonic generation in a GaP waveguide. *Appl. Phys. Lett.* **1975**, *27*, 71 – 73.
- (4) Rivoire, K.; Buckley, S.; Hatami, F.; Vučković, J. Second harmonic generation in GaP photonic crystal waveguides. *Appl. Phys. Lett.* **2011**, *98*, 263113.
- (5) Helmy, A. S.; Abolghasem, P.; Stewart Aitchison, J.; Bijlani, B. J.; Han, J.; Holmes, B. M.; Hutchings, D. C.; Younis, U.; Wagner, S. J. Recent advances in phase matching of second-order nonlinearities in monolithic semiconductor waveguides. *Laser and Photonics Rev.* **2011**, *5*, 272 – 286.
- (6) Sanatinia, R.; Swillo, M.; Anand, S. Surface second-harmonic generation from vertical GaP nanopillars. *Nano Lett.* **2012**, *12*, 820 – 826.
- (7) Václavík, J.; Vápenka, D. Gallium Phosphide as a material for visible and infrared optics. EPJ Web of Conferences. 2013.
- (8) Sanatinia, R.; Anand, S.; Swillo, M. Modal engineering of second-harmonic generation in single GaP nanopillars. *Nano Lett.* **2014**, *14*, 5376 – 5381.
- (9) Guha, S.; Barnes, J. O.; Schunemann, P. G. Mid-wave infrared generation by difference frequency mixing of continuous wave lasers in orientation-patterned Gallium Phosphide. *Opt. Mater. Express* **2015**, *5*, 2911 – 2923.
- (10) Sanatinia, R.; Anand, S.; Swillo, M. Experimental quantification of surface optical nonlinearity in GaP nanopillar waveguides. *Opt. Express* **2015**, *23*, 756 – 764.
- (11) Ye, H.; Chaitanya Kumar, S.; Wei, J.; Schunemann, P. G.; Ebrahim-Zadeh, M. Optical parametric generation in orientation-patterned gallium phosphide. *Opt. Lett.* **2017**, *42*, 3694 – 3697.
- (12) Logan, A. D.; Gould, M.; Schmidgall, E. R.; Hestroffer, K.; Lin, Z.; Jin, W.; Majumdar, A.; Hatami, F.; Rodriguez, A. W.; Fu, K.-M. C. 400%/W second harmonic

- conversion efficiency in 14  $\mu\text{m}$ -diameter gallium phosphide-on-oxide resonators. *Opt. Express* **2018**, *26*, 33687 – 33699.
- (13) Schneider, K.; Welter, P.; Baumgartner, Y.; Hahn, H.; Czornomaz, L.; Seidler, P. Gallium Phosphide-on-Silicon Dioxide Photonic Devices. *J of Lightw. Technol.* **2018**, *36*, 2994 – 3002.
- (14) Cambiasso, J.; Grinblat, G.; Li, Y.; Rakovich, A.; Cortés, E.; Maier, S. A. Bridging the Gap between Dielectric Nanophotonics and the Visible Regime with Effectively Lossless Gallium Phosphide Antennas. *Nano Lett.* **2017**, *17*, 1219 – 1225.
- (15) Poulvellarie, N.; Dave, U.; Alexander, K.; Ciret, C.; Raineri, F.; Combrié, S.; De Rossi, A.; Roelkens, G.; Gorza, S.-P.; Kuyken, B.; Leo, F. Second Harmonic Generation Induced by Longitudinal Components in Indium Gallium Phosphide Nanowaveguides. NLO. 2019; p NM3B.2.
- (16) Wilson, D. J.; Schneider, K.; Hoehl, S.; Anderson, M.; Kippenberg, T. J.; Seidler, P. Integrated gallium phosphide nonlinear photonics. *Nat. Photon.* **2019**, doi: 10.1038/s41566-019-0537-9.
- (17) Franken, P. A.; Hill, A. E.; Peters, C. W.; Weinreich, G. Generation of optical harmonics. *Phys. Rev. Lett.* **1961**, *7*, 118 – 119.
- (18) Armstrong, J. A.; Bloembergen, N.; Ducuing, J.; Pershan, P. S. Interactions between light waves in a nonlinear dielectric. *Phys. Rev.* **1962**, *127*, 1918 – 1939.
- (19) Robert W. Boyd, *Nonlinear optics*, 4th ed.; Academic Press, 2019.
- (20) Armstrong, J. A. Measurement of picosecond laser pulse widths. *Appl. Phys. Lett.* **1967**, *10*, 16 – 18.
- (21) T. F. Heinz, C. K. Chen, D. Ricard,; Shen, Y. R. Spectroscopy of Molecular Monolayers by Resonant Second-Harmonic Generation. *Phys. Rev. Lett.* **1982**, *48*, 478 – 481.

- (22) Freund, I.; Deutsch, M. Second-harmonic microscopy of biological tissue. *Opt. Lett.* **1986**, *11*, 94 – 96.
- (23) Karsten Rottwitt, Peter Tidemand-Lichtenberg, *Nonlinear optics: Principles and Applications*, 1st ed.; CRC Press, 2014.
- (24) Fathpour, S. Heterogeneous nonlinear integrated photonics. *IEEE J. of Quantum Electron.* **2018**, *54*, 6300716.
- (25) Minzioni, P. et al. Roadmap on all-optical processing. *J. Opt.* **2019**, *21*, 063001.
- (26) <http://www.gwoptics.org/ComponentLibrary/>.
- (27) Neradovskiy, M.; Neradovskaia, E.; Chezganov, D.; Vlasov, E.; Shur, V. Y.; Tronche, H.; Doutre, F.; Ayenew, G.; Baldi, P.; De Micheli, M.; Montes, C. Second harmonic generation in periodically poled lithium niobate waveguides with stitching errors. *J. Opt. Soc. Am. B* **2018**, *35*, 331 – 336.
- (28) <https://www.hcphotonics.com/ppln-guide-overview>.
- (29) Kelley Rivoire, Ziliang Lin, Fariba Hatami, W. Ted Masselink,; Vuckovic, J. Second harmonic generation in gallium phosphide photonic crystal nanocavities with ultralow continuous wave pump power. *Opt. Express* **2009**, *17*, 22610 – 22615.
- (30) Bruch, A. W.; Liu, X.; Guo, X.; Surya, J. B.; Gong, Z.; Zhang, L.; Wang, J.; Yan, J.; Tang, H. X. 17 000%/W second-harmonic conversion efficiency in single-crystalline aluminum nitride microresonators. *Appl. Phys. Lett.* **2018**, *113*, 131102.
- (31) Chang, L.; Boes, A.; Guo, X.; Spencer, D. T.; Kennedy, M. J.; Peters, J. D.; Volet, N.; Chiles, J.; Kowligy, A.; Nader, N.; Hickstein, D. D.; Stanton, E. J.; Diddams, S. A.; Papp, S. B.; Bowers, J. E. Heterogeneously Integrated GaAs Waveguides on Insulator for Efficient Frequency Conversion. *Laser Photonics Rev.* **2018**, *12*, 1800149.

- (32) Luo, R.; He, Y.; Liang, H.; Li, M.; Lin, Q. Highly tunable efficient second-harmonic generation in a lithium niobate nanophotonic waveguide. *Optica* **2018**, *5*, 1006 – 1011.
- (33) Boes, A.; Chang, L.; Knoerzer, M.; Nguyen, T. G.; Peters, J. D.; Bowers, J. E.; Mitchell, A. Improved second harmonic performance in periodically poled LNOI waveguides through engineering of lateral leakage. *Opt. Express* **2019**, *27*, 23919 – 23928.
- (34) May, S.; Keus, M.; Clerici, M.; Sorel, M. Second-harmonic generation in AlGaAs-on-insulator waveguides. *Opt. Lett.* **2019**, *44*, 1339 – 1342.
- (35) Luo, R.; He, Y.; Liang, H.; Li, M.; Ling, J.; Lin, Q. Optical Parametric Generation in a Lithium Niobate Microring with Modal Phase Matching. *Phys. Rev. Appl.* **2019**, *11*.
- (36) Chang, L.; Li, Y.; Volet, N.; Wang, L.; Peters, J.; Bowers, J. E. Thin film wavelength converters for photonic integrated circuits. *Optica* **2016**, *3*, 531 – 535.
- (37) Chen, J.-Y.; Sua, Y. M.; Fan, H.; Huang, Y.-P. Modal phase matched lithium niobate nanocircuits for integrated nonlinear photonics. *OSA Continuum* **2018**, *1*, 229 – 242.
- (38) Chowdhury, A.; Ng, H. M.; Bhardwaj, M.; Weimann, N. G. Second-harmonic generation in periodically poled GaN. *Appl. Phys. Lett.* **2003**, *83*, 1077 – 1079.
- (39) Duchesne, D.; Rutkowska, K. A.; Volatier, M.; Légaré, F.; Delprat, S.; Chaker, M.; Modotto, D.; Locatelli, A.; De Angelis, C.; Sorel, M.; Christodoulides, D. N.; Salamo, G.; Arès, R.; Aimez, V.; Morandotti, R. Second harmonic generation in AlGaAs photonic wires using low power continuous wave light. *Opt. Express* **2011**, *19*, 12408 – 12417.
- (40) Rutkowska, K. A.; Duchesne, D.; Volatier, M.; Arès, R.; Aimez, V.; Morandotti, R. Second harmonic generation in AlGaAs nanowaveguides. *Acta Phys. Pol. A* **2011**, *120*, 725 – 731.

- (41) Yamada, M.; Nada, N.; Saitoh, M.; Watanabe, K. First-order quasi-phase matched LiNbO<sub>3</sub> waveguide periodically poled by applying an external field for efficient blue second-harmonic generation. *Appl. Phys. Lett.* **1993**, *62*, 435 – 436.
- (42) Gromovyi, M.; Brault, J.; Courville, A.; Rennesson, S.; Semond, F.; Feuillet, G.; Baldi, P.; Boucaud, P.; Duboz, J.-Y.; De Micheli, M. P. Efficient second harmonic generation in low-loss planar GaN waveguides. *Opt. Express* **2017**, *25*, 23035 – 23044.
- (43) Lake, D. P.; Mitchell, M.; Jayakumar, H.; Dos Santos, L. F.; Curic, D.; Barclay, P. E. Efficient telecom to visible wavelength conversion in doubly resonant gallium phosphide microdisks. *Appl. Phys. Lett.* **2016**, *108*, 031109.
- (44) Stefszky, M.; Ricken, R.; Eigner, C.; Quiring, V.; Herrmann, H.; Silberhorn, C. High-power waveguide resonator second harmonic device with external conversion efficiency up to 75%. *J. Opt.* **2018**, *20*, 065501.
- (45) Rao, S. V.; Moutzouris, K.; Ebrahimzadeh, M. Nonlinear frequency conversion in semiconductor optical waveguides using birefringent, modal and quasi-phase-matching techniques. *J. Opt. A-Pure Appl. Op.* **2004**, *6*, 569 – 584.
- (46) Wang, C.; Li, Z.; Kim, M. H.; Xiong, X.; Ren, X. F.; Guo, G. C.; Yu, N.; Lončar, M. Metasurface-assisted phase-matching-free second harmonic generation in lithium niobate waveguides. *Nat. Commun.* **2017**, *8*:2098.
- (47) Wang, C.; Xiong, X.; Andrade, N.; Venkataraman, V.; Ren, X.-F.; Guo, G.-C.; Lončar, M. Second harmonic generation in nano-structured thin-film lithium niobate waveguides. *Opt. Express* **2017**, *25*, 6963 – 6974.
- (48) Abolghasem, P.; Han, J.; Bijlani, B. J.; Arjmand, A.; Helmy, A. S. Highly efficient second-harmonic generation in monolithic matching layer enhanced Al<sub>x</sub>Ga<sub>1-x</sub>As Bragg reflection waveguides. *IEEE Photon. Technol. Lett.* **2009**, *21*, 1462 – 1464.

- (49) Fiore, A.; Janz, S.; Delobel, L.; Van Der Meer, P.; Bravetti, P.; Berger, V.; Rosencher, E.; Nagle, J. Second-harmonic generation at  $\lambda=1.6 \mu\text{m}$  in AlGaAs/Al<sub>2</sub>O<sub>3</sub> waveguides using birefringence phase matching. *Appl. Phys. Lett.* **1998**, *72*, 2942 – 2944.
- (50) Moutzouris, K.; Rao, S. V.; Ebrahimzadeh, M.; De Rossi, A.; Berger, V.; Calligaro, M.; Ortiz, V. Efficient second-harmonic generation in birefringently phase-matched GaAs Al<sub>2</sub>O<sub>3</sub> waveguides. *Opt. Lett.* **2001**, *26*, 1785 – 1787.
- (51) Scaccabarozzi, L.; Fejer, M. M.; Huo, Y.; Fan, S.; Yu, X.; Harris, J. S. Enhanced second-harmonic generation in AlGaAs/ Al<sub>x</sub>O<sub>y</sub> tightly confining waveguides and resonant cavities. *Opt. Lett.* **2006**, *31*, 3626 – 3628.
- (52) Pernice, W. H. P.; Xiong, C.; Schuck, C.; Tang, H. X. Second harmonic generation in phase matched aluminum nitride waveguides and micro-ring resonators. *Appl. Phys. Lett.* **2012**, *100*, 223501.
- (53) Guo, X.; Zou, C.-L.; Tang, H. X. Second-harmonic generation in aluminum nitride microrings with 2500%/W conversion efficiency. *Optica* **2016**, *3*, 1126 – 1131.
- (54) Ge, L.; Chen, Y.; Jiang, H.; Li, G.; Zhu, B.; Liu, Y.; Chen, X. Broadband quasi-phase matching in a MgO:PPLN thin film. *Photonics Research* **2018**, *6*, 954 – 958.
- (55) Cai, L.; Wang, Y.; Hu, H. Efficient second harmonic generation in  $\chi(2)$  profile reconfigured lithium niobate thin film. *Opt. Commun.* **2017**, *387*, 405 – 408.
- (56) Yariv, A. Coupled-Mode Theory for Guided-Wave Optics. *IEEE J. of Quantum Electron.* **1973**, *QE-9*, 919 – 933.
- (57) Shoji, I.; Kondo, T.; Kitamoto, A.; Shirane, M.; Ito, R. Absolute scale of second-order nonlinear-optical coefficients. *J. Opt. Soc. Am. B* **1997**, *14*, 2268 – 2294.

- (58) Kuo, P. S.; Fejer, M. M. Mixing of polarization states in zincblende nonlinear optical crystals. *Opt. Express* **2018**, *26*, 26971 – 26984.
- (59) U. Dave, N. Poulvellarie, K. Alexander, S.-P. Gorza, F. Raineri, S. Combri'e, A. De Rossi, G. Roelkens, B. Kuyken,; Leo, F. Second Harmonic Generation by Mixing Longitudinal and Transverse Electric Field Components in Indium Gallium Phosphide-on-insulatorWire Waveguides. Advanced Photonics Congress (BGPP, IPR, NP, Networks, NOMA, Sensors, SOF, SPPCom). 2018.